Viscous and capillary pressures during drainage: Network simulations and experiments

S. C. van der Marck, T. Matsuura, and J. Glas
SIEP Research and Technical Services, P.O. Box 60, 2280 AB Rijswijk, The Netherlands
(Received 8 November 1996; revised manuscript received 3 June 1997)

The displacement of a wetting fluid by a nonwetting fluid in a porous medium, i.e., drainage, was studied by means of experiments and simulations. A network model was formulated, capable of describing the fluid saturation of the porous medium and the pressure during the displacement. The results of experiments with several micro flow models are reported, using two fluid systems and varying displacement rates. These measurements allow interpretation in terms of the contributions of the capillary and viscous pressures. The results of the simulations are in agreement with the experiments, with the exception of one case at a high displacement rate and characterized by a high viscosity ratio. [S1063-651X(97)13310-4]

PACS number(s): 47.55.Mh, 47.11.+j, 47.55.Kf, 68.45.Gd

I. INTRODUCTION

Immiscible two-phase flow in porous media has applications in a wide variety of technological areas, such as oil recovery, soil reconstitution processes, wetting and drying processes, and hydrology. Although immiscible flow can take place in many forms, the work reported in this paper is restricted to the study of two-phase displacement processes. In particular, we were interested in the so-called drainage process, where the nonwetting fluid displaces the wetting one (the reverse process is called imbibition). On a macroscopic scale, the generalized Darcy equations are used to describe these phenomena [1,2]. However, these equations are of a semi-empirical nature, and require several experimental parameters as input, such as capillary pressure curves and relative permeabilities. One would like to have a more fundamental understanding of how these semiempirical, macroscopic equations, and the quantities appearing in them, relate to the well-known laws of fluid dynamics and to the microscopic description of the porous material.

Network models have been developed to describe fluid flow through porous media on a microscopic scale. By close analogy with random resistor networks, single phase flow can be described by a network of capillaries, connecting the pores [3–5]. Each capillary in the network is assigned a flow conductance, which relates the flow rate through the capillary to the pressure drop over it. By imposing fluid conservation at each pore, one arrives at a set of equations similar to Kirchhoff's equations for random resistor networks. If the network is representative of a porous medium [6,7], one can calculate the permeability [8,9]. On applying this network model in two-phase flow, the introduction of the capillary pressure difference between the two phases poses a difficult problem. So far two limiting cases have been described in the literature. In the first one the capillary forces are dominant over the viscous forces. When the the viscous pressure drop can be neglected, the invasion percolation model [10–13] gives a good description of drainage [14]. A second limiting case is found in situations where the viscous forces are dominant over the capillary forces: the diffusion limited aggregation (DLA) model describes the displacement of a high-viscosity fluid by a low-viscosity fluid, thereby giving rise to viscous fingering [15–17].

Both the invasion percolation and the DLA network models are built on ''rules.'' DLA, for instance, involves random walkers obeying a set of rules that determine how the walkers traverse the network. If one wishes to describe drainage in the more general situation, where capillary and viscous forces are both present, these rule-based models should be combined in some form or other with the random resistor type model. For this, one can use a rule based model to update the fluid configuration and then perform a random resistor type calculation to determine the pressure drop in one of the fluids, while immobilizing the other fluid [18–21]. Although this model gives interesting results, it does not describe the transition from capillary dominated drainage to viscous dominated drainage, since the viscous pressure drop is not taken into account when updating the fluid configuration.

Several attempts have been made to combine these models with the random resistor type models. The differences between the various methods lie mainly in the way in which the network is set up. Payatakes and co-workers, for example, use a network in which there are only channels [22,23]. These channels have a sinusoidal shape and represent both pores and pore throats of a porous medium. Another approach is to use spheres for the pores and cylinders for the channels, as was done by Koplik and Lasseter [3]. Lenormand *et al.* [24,25] presented a simplification, using pores that are mere fluid reservoirs (having only volume) and channels, which carry no volume, but represent the flow properties of the network. The advantage of such a network model is that simulations are less laborious than when using the networks that were mentioned earlier.

However, in these publications, the pressure field that is predicted by the simulations for a flow controlled displacement was not accounted for. But this is just as important a physical parameter as the saturation. Although the saturation is more directly related to, e.g., the recovery factor for an oil reservoir, it is the pressure buildup that determines the displacement of one fluid by another. The interplay between pressure buildup and fluid displacement remains incomprehensible as long as these factors are not described accurately by simulation.

We have used a network model similar to the one introduced by Lenormand *et al.* to compute the pressure field.

However, we found that we had to extend the rules used in his model to obtain a satisfactory description of the pressure during drainage. We also performed experiments in micro flow models, in which we measured the local fluid pressure. These are measurements of the local fluid pressure during flow controlled displacement. Lenormand recorded pressure differences in a pressure controlled displacement experiment, with negligible viscous pressures [24]. Avraam and Payatakes also determined pressures in a micro flow model [26], but they measured an average over several pores, and hence also over the two fluids. In our investigation, we have measured the pressures in the two fluids separately, permitting the interpretation of the viscous and capillary contributions to the pressure difference in the model.

We have formulated our network model in Sec. II. Some of the details are deferred to the two appendices, viz., the flow properties of channels to Appendix A and the full network equations and update rules to Appendix B. In Sec. III we have described our micro flow models and our procedure to make them. In Sec. IV the experimental setup and procedure are described. In Sec. V we present our measurements of drainage pressure curves in several micro flow models, using two fluid systems. The first fluid system had a viscosity ratio of 1 (unity), whereas in the second fluid system the nonwetting fluid was about twelve times more viscous than the wetting fluid (viscosity ratio ~ 12). The difference between the micro flow models was mainly one of topology. The coordination number of the models ranged from 3 to 5. The model with coordination number 5 had a nonplanar structure. The results of the measurements are compared with simulations, whereby we have focused on the pressure buildup during the displacement. In most cases the simulations are in agreement with the experiments. Only in a case with a high-viscosity ratio was the pressure buildup underestimated, using the simulations, although the saturation curve matched the experimental one.

II. THE NETWORK MODEL

In this section we present our network simulator. It is an extension of the model introduced by Lenormand *et al.* [8,9,24,25]. Lenormand and co-workers were primarily concerned with the invasion pattern of a nonwetting fluid into a porous medium filled with a wetting phase. The pressure of the nonwetting fluid during flow controlled displacement was not studied. For an accurate description of the pressure of a nonwetting phase one needs to extend the ''rules'' of the original network model.

For complicated systems, one has to make certain simplifications to keep the model effective. The main assumptions that have been introduced into our model are the following: (i) the flow is in the Stokes regime, i.e., inertial effects can be neglected; (ii) the fluids are Newtonian, incompressible and immiscible; (iii) the pores are reservoirs without any flow properties; (iv) the channels have no volume, but carry a fluid label, indicating which fluid is flowing through the channel; (v) the geometry and the dimensions of the channels determine the flow properties of the network.

When the flow is in the Stokes regime, the flow behavior of the fluids is determined by three forces, viz., the viscous, capillary, and gravitational forces. In the simulator all of these are taken into account. We shall discuss each of them separately, starting with the viscous force.

Each channel in the network is assigned a flow conductance, the value of which is determined by its geometrical properties. The flow conductance c_{ij} determines the flow rate in a channel between pores labeled by i and j, which are at pressures p_i and p_j, respectively, in the following way:

$$Q_{ij}=\frac{c_{ij}}{\mu_{ij}}(p_i-p_j), \tag{1}$$

where Q_{ij} is the amount of fluid flowing from pore i to pore j per unit of time and μ_{ij} is the viscosity of the fluid in the channel. For the calculation of the flow conductance c_{ij} it is assumed that the flow in a channel can be described by a Poiseuille flow. The flow in the channels is treated as a single phase flow problem; neither film nor corner flow have been implemented in the simulator. This may be one of the more limiting simplifications made in this model.

The capillary force causes a pressure difference between the oil (nonwetting) and the water (wetting fluid). If the interface between the oil and water is characterized by a mean radius of curvature R_c, the pressure difference is given by (Ref. [2], p. 8)

$$p_{nw}-p_w=\frac{2\sigma\cos\vartheta}{R_c}, \tag{2}$$

where p_{nw} and p_w are the pressures of the nonwetting and wetting fluids, σ is the interfacial tension between the fluids, and ϑ is the contact angle. Capillary effects, due to interfaces in the pores, are considered to be negligible, and only interfaces at the boundaries between a pore and channel and in the channels themselves are taken into account. For this purpose each channel was assigned a capillary entry pressure P^e_{ij}, which is the pressure difference between oil and water that is needed for the oil to enter a water filled channel. For example, if pore i is filled with oil and pore j with water, the oil will only enter the channel between the pores if $p_i-p_j>P^e_{ij}$. This means that the channel can be ''capillary blocked,'' i.e., there will be no flow in the channel when $0\leqslant p_i-p_j\leqslant P^e_{ij}$.

Furthermore, gravity gives rise to a hydrostatic pressure gradient. The pressure difference between pores i and j at positions $\mathbf{x}_i$ and $\mathbf{x}_j$, respectively, is given by

$$p_i-p_j=\rho_{ij}\mathbf{g}\cdot(\mathbf{x}_i-\mathbf{x}_j), \tag{3}$$

where ρ_{ij} is the density of the fluid in the channel connecting pores i and j and $\mathbf{g}$ is the acceleration due to gravity.

The values of the flow conductance c_{ij} and the entry pressure P^e_{ij} depend on the geometry and the sizes of the channel between pores i and j. A type of geometry that resembles a channel in our micro flow models was implemented in our simulator (see Fig. 1). In Appendix A we give the formulas of c_{ij} and P^e_{ij} for this type of channel.

The fluid flow through a channel is determined by the interaction of the three forces discussed above. We have distinguished between configurations with zero, one, or two menisci in a channel (see Fig. 2). (1) If no meniscus is present

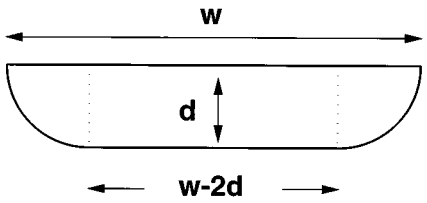

FIG. 1. The geometry of a channel as assumed in the simulator.

in the channel then

$$Q_{ij}=\frac{c_{ij}}{\mu_{ij}}(p_i-p_j). \tag{4}$$

(2) If one meniscus is present, and pore i is filled with oil, and pore j is filled with water then

$$Q_{ij}=\frac{c_{ij}}{\mu_{ij}}\{\theta(p_j-p_i)(p_i-p_j) + \theta(p_i-p_j-P^e_{ij})(p_i-p_j-P^e_{ij})\}, \tag{5}$$

where the Heaviside function $\theta(x)$ is defined by

$$\theta(x)=\begin{cases}1 & \text{if } x>0\\ 0 & \text{otherwise.}\end{cases} \tag{6}$$

If $p_i<p_j$, water will flow from pore j to pore i. If $p_i-p_j>P^e_{ij}$, oil will flow from pore i to pore j. In other cases the channel is capillary blocked. (3) If two menisci are present, and pores i and j are filled with oil, and the channel is filled with water then

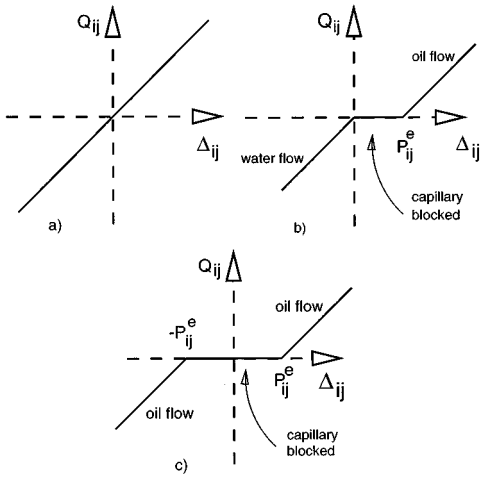

FIG. 2. The three flow configurations that are taken into account in the simulator. (a) Corresponds to absence of a meniscus in the channel [Eq. (4)], (b) corresponds to one meniscus present in the channel [Eq. (5)], and (c) to two menisci [Eq. (7)]. The flow in the channel between pore i and pore j is denoted by Q_{ij}. The variable Δ_{ij} is equal to $p_i-p_j-\rho_{ij}\mathbf{g}\cdot(\mathbf{x_i}-\mathbf{x_j})$. The entry pressure of the channel is P^e_{ij}.

$$Q_{ij}=\frac{c_{ij}}{\mu_{ij}}\{\theta(p_j-p_i-P^e_{ij})(p_i-p_j+P^e_{ij}) + \theta(p_i-p_j-P^e_{ij})(p_i-p_j-P^e_{ij})\}. \tag{7}$$

If $p_j-p_i>P^e_{ij}$, oil will flow from pore j to pore i. If $p_i-p_j>P^e_{ij}$, oil will flow from pore i to pore j. In all other cases the channel will be capillary blocked. It can be seen that the capillary force gives rise to nonlinear flow equations.

In the formulas shown above, we have excluded the gravity terms. These can be incorporated by replacing in Eqs. (4)–(7) p_i-p_j by $p_i-p_j-\rho_{ij}\mathbf{g}\cdot(\mathbf{x}_i-\mathbf{x}_j)$.

So far we have only looked at the relation between the flow rate through a single channel and the pressure difference between the pores that are connected by the channel. However, we wish to determine the behavior of the fluids in the whole network consisting of many pores and channels. In order to derive the equations that represent the fluid flow through a network we made use of the fact that we were dealing with incompressible fluids. This means that the total volume of the fluids is conserved, i.e., the net fluid in-flux into each pore is zero. Therefore, one may write for each pore i

$$Q^e_i=\sum_j Q_{ij}, \tag{8}$$

where Q^e_i is the external influx into pore i, which is zero unless the pore happens to be a boundary one, and the sum runs over all neighboring pores. Replacing Q_{ij} by the expressions given in Eqs. (4)–(7) one obtains a set of nonlinear equations. In Appendix B we have given the explicit form of the equations. The differences between the present work and the approach of Lenormand *et al.* [24,25] is described in detail at the end of Appendix B. The set of nonlinear equations may be solved numerically, yielding the pressure at each pore of the network.

A typical simulation consists of the following steps (it is similar to what is known in reservoir engineering as the implicit pressure, explicit saturation (IMPES) scheme [27]):

(1) A fluid configuration and the boundary conditions are defined. In our simulations we impose flow rates at the inlet pores and pressures at the outlet pores.

(2) The fluid configuration determines which of the equations (4)–(7) should be selected for each channel. A more detailed description of this procedure is given in Appendix B.

(3) The network equations given in Eq. (8) are applied. This results in a calculation of the pressure field over the network.

(4) From the pressure field solution in step (3) one can determine for each channel the identity of the fluid that is flowing through it (oil or water, or capillary blocked) and its flow rate.

(5) Determine the size of the time step. For each pore one calculates the time needed to get completely filled with either oil or water (depending which of the two has a positive net in-flux). The minimum of these times is taken as the size of the next time step. It is assumed that during a time step the pressure field over the network does not change.

(6) The saturation of all pores is updated using the flow rates determined in step (4) and the time step determined in step (5). This results in a new fluid configuration.

(7) Go back to step (2) unless some predefined stop criterion is reached.

Repeating the steps described above two-phase flow through a network can be simulated. At this moment the model will only give acceptable results for cases where the oil saturation in the network increases with time (drainage type simulation). The main reason for this is that film or corner flow plays a much more important role when imbibition occurs. The inclusion of film flow will necessitate an extension of Eqs. (4)–(7). Moreover, imbibition calls for more sophisticated update rules than the ones used in the present simulator.

In the discussion above no restrictions were imposed on the topology of the network. The simulator can handle any topology for the network (two- and three-dimensional and any desired coordination number). One only has to specify how the pores are connected to each other.

In the limit of vanishing flow rate, the current model is reduced to invasion percolation. There is, however, a subtle difference between the two models, even in this extreme condition. In the current model, several pores can be filled simultaneously during a time step, in contrast to invasion percolation. This should not be of importance, however, unless the network is degenerate, containing many equal-sized channels. We found that, when the drainage front is gravity stabilized, the results of the current model converged with those from invasion percolation. Due to numerical problems we were unable to choose sufficiently low flow rates under nonstabilized conditions.

III. THE MICRO FLOW MODELS

Experiments were performed in four glass micro flow models. One of these consisted of a two-layer micro flow system (see Fig. 3), the other three were one-layer models. The width w of the channels in each of these models was designed to be either 96, 127, or 165 μm, based on a random selection for each individual channel. Variations in conditions during etching and fusing of the models gave an estimated range of 5 μm around these values. The pores were made with diameters of 232, 268, and 304 μm, respectively, again with a range of 5 μm above or below this value. The channel length, defined from pore center to pore center, was 1 mm in model M1, and 0.57 mm in the other models.

The charactistics of the various models were as follows:

Model M1. This model was a two-layer model, consisting of three glass plates, where in the top plate (red in Fig. 3) and in the bottom one (blue in Fig. 3) a square pattern of pores and channels was etched and in the middle plate (black in Fig. 3) connections were made to interconnect with the other two. The result was topologically the same as a $25\times25\times2$ cubic network. The model had 1250 pores and 3075 channels; the etching depth was 35 μm.

Model M2. This model was a one-layer model, where in one glass plate a 49×49 square network of pores and channels was etched. The other glass plate contained a mirror image of the first and was fused on top of it. The model consisted of 4704 channels, and 2401 pores; the etching depth was 30 μm.

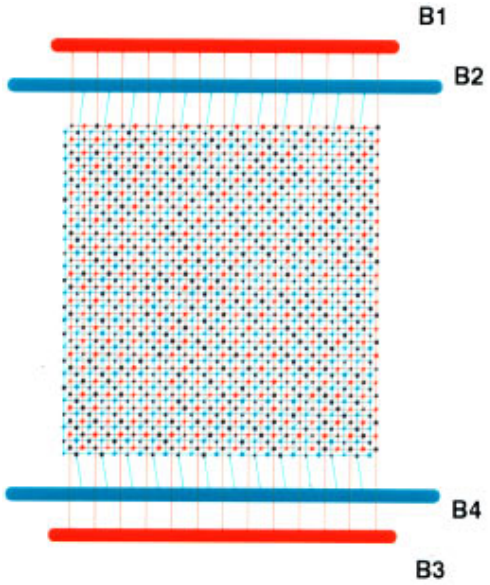

FIG. 3. (Color). The design pattern of the two-layer micro flow model M1; the top layer is depicted in red, the bottom one in blue, and the connections between the two in black.

Model M3. This model resembled M2, but the channels were etched in one of the glass plates only, whereas the pores were etched in both plates. Hence M3 had a higher ratio of pore size divided by channel size (''aspect ratio'') than M2, and a lower fluid conductance. The galleries and the channels connecting them to the model were etched in both glass plates; the etching depth was 35 μm.

Model M4. This model also resembled M2, but 1219 randomly selected channels were removed. The model had 2401 pores and 3485 channels, and hence the connectivity of M4 was lower than that of M2. The model was designed in such a way that each pore would have at least two channels connected to it (see Fig. 4). The etching depth was 35 μm, but during fusing the model was kept in the oven too long, which resulted in a lower channel depth. A comparison with single phase flow simulations suggested that the channel depth after fusing was roughly 2×20 μm.

The wide structures at the top and bottom of Fig. 3, labeled B1 through B4, were named galleries. These galleries were made deeper than the rest of the etched pattern by sawing.

We shall briefly describe the construction of the two-layer model, because it is partly new. Three glass plates of 2 mm thickness were used for the construction. On two glass plates a planar pore network was etched (the red and the blue network of Fig. 3) and on the third one holes were etched that served as channels connecting the two network layers (the black dots in Fig. 3). The lithographic technique by which the glass plates were etched was as follows. A thin layer of copper was applied to one side of each glass plate using a vacuum-deposition technique. The copper surface was covered with a layer of photoresistant material. A negative film of the computer-drawn template of the pore network was pressed against the photoresistant layer, and the device was then exposed to UV light. After the photoresist was developed, the glass plates were baked in an oven at 185 °C to ''harden'' the remaining photoresist. Next, the exposed copper was dissolved in a weak solution of ferrichloride

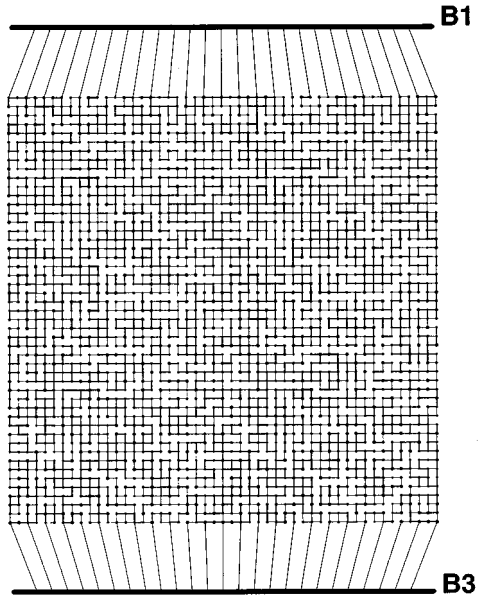

FIG. 4. The design pattern of the single-layer micro flow model M4; a square pattern with roughly a quarter of the channels removed.

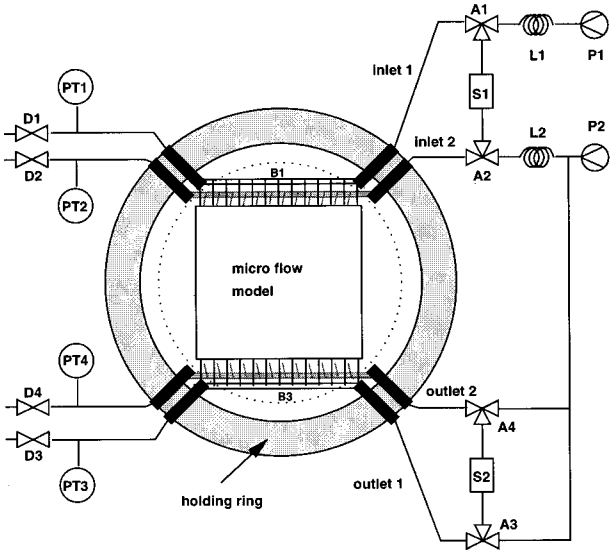

FIG. 5. A schematic representation of the experimental setup.

($FeCl_3$). The glass surface exposed through this treatment was then acid-etched in an aqueous solution of $NH_4 \cdot HF$ (250 g/l) in the following three-step cycle: (1) etching during roughly 2.5 min; (2) Submersion of the glass plates in water for 1 min; (3) Removal of the insoluble residue, which remained after etching, by washing the glass plates in a saturated solution of soda in water. This cycle was repeated until the depth of the etched areas was 35 μm for the plates with the pore networks, and 50 μm for the plate with the holes. After etching, the three glass plates were fused in two stages. First, the plate with the holes and one of the other plates were aligned under a microscope to ensure that the holes coincided perfectly with the chambers of the planar network; the two plates were then fused in a furnace at 625 °C under mild mechanical pressure. Before the third plate was riveted onto the other side of the hole plate, the hole plate had to be ground to a thickness of 50 μm so that the holes extended from one side of the plate to the other. Grinding was a delicate enterprise. Before grinding, the model was filled with wax, to ensure that no glass particles were left in the pores. When the desired thickness of 50 μm was reached, the wax was removed and the glass surface was carefully cleaned and polished. Then the third glass plate was fused onto the device as described above.

TABLE I. Fluid properties (at $T = 32.7$ °C); IFT stands for interfacial tension with respect to water.

	Nonwetting 1	Nonwetting 2	Wetting
Description	*n*-decane	Vitrea-9	Water
Dye (saturated)	Sudan Red IV	Sudan Red IV	None
Viscosity (mPa s)	0.78	9.4	0.78
density (kg/m^3)	721	871	995
IFT (mN/m)	36.2	31.3	

IV. THE EXPERIMENTS

A glass model was clamped between glass disks in a holder with eight flow ports, that were connected to the ends of the galleries via flow conduits in the glass disks (see Fig. 5). In this setup the micro flow model was mounted in a vertical position. In the case of a one-layer model there were two galleries and only four ports were connected to flow lines. The sample holder was suspended in a temperature controlled bath, at 32.7 °C.

The schematics of the experimental setup for a two-layer model is given in Fig. 5. The two inlet flow lines were connected to B1 and B2 (see Fig. 3). The outlets of the model (B3 and B4 in Fig. 3) were connected to the outlet flow lines, leading to the syphon S2. There were four pressure transducers PT1 to 4 (range -219 to $+219$ mbar), four ball valves D1 to 4, two Valco three-way selection valves A1 and A2, two Whitey three-way selection valves A3 and A4, and two oil loops L1 and L2 with their Valco valves. The position of the pressure transducers was such that they measured the static pressure in the lines during an experiment. ISCO syringe pumps supplied the pressure.

The water used for the experiments was deionized, then passed through a Millipore Milli-Q purifying apparatus, and subsequently boiled to remove the air. The oil was stored in the loops L1 and L2, and when a drainage experiment was performed it was driven out by the water into the micro flow model. The course of an experiment was recorded in the following manner: pressures and flow rates were read in by a data acquisition program, and oil saturation was determined by digital analysis of slides taken during the experiment. The digitalisation of the slides was done by Kodak at a resolution of 3192×2048, full color. The analysis of these images was performed with a special purpose program, which identified the contents of each pore and channel.

After an experiment we cleaned the apparatus thoroughly. It involved flushing with IPA and water, usually for one night. When the model required an even more thorough

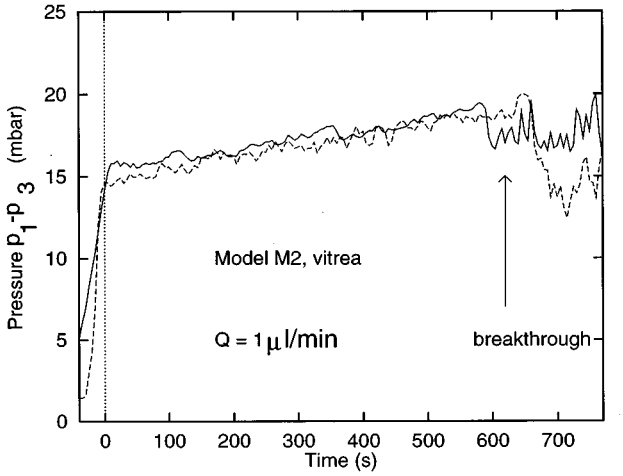

FIG. 6. An experimental pressure curve for drainage with Vitrea-9 in model M2, showing the reproducibility.

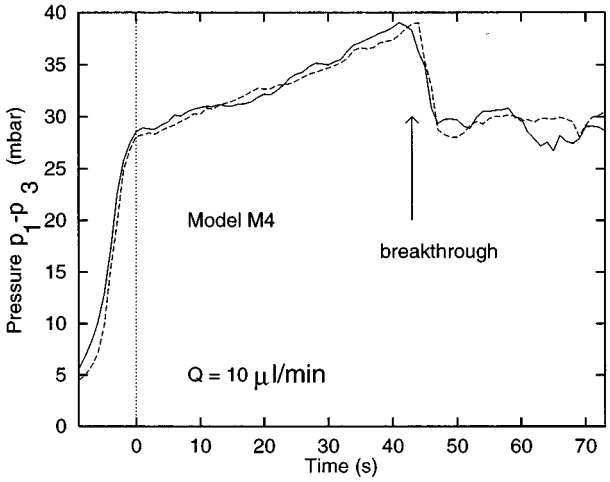

FIG. 7. An experimental pressure curve for drainage with *n*-decane in model M4, showing the reproducibility.

cleaning, it was heated to 450 °C.

For most of the experiments we used *n*-decane as nonwetting fluid, in which the dye Sudan Red IV was dissolved. In model M2 we also used Vitrea-9 [28] to test the influence of an increase in the viscosity ratio. The properties of these fluid systems are listed in Table I. The surface tension and the interfacial tension were measured using the Du Nouy ring method. The viscosity of Vitrea-9 was measured with the ubbelohde method (Schott Geräte viscometer, type AVS 310) and the density was determined with a Mettler/Paar densitometer (type DMA 55). The contact angles were estimated to be about 30°.

The case of a viscosity ratio lower than 1 was not considered, because it does not occur often. In the oil industry, for instance, the oils are usually more viscous than water. Moreover the displacement tends to get unstable when the displacing fluid is less viscous than the displaced one (as is the case for DLA). Numerically this is also more complicated.

With each of the models we performed flow rate controlled drainage experiments at least twice, to ensure reproducibility. Oil was injected at a fixed flow rate into the water filled micro flow model. The pressure curves followed a fixed pattern. See, e.g., Figs. 6 and 7, where we plotted the pressure curves for several experiments to show the reproducibility. (We made sure that the saturation profiles were also reproducible.)

At first the pressure had to increase to the value of the capillary entry pressure of the model. After the oil had entered the system, the pressure rose slowly, due to an increase in the viscous pressure drop. This increase was caused by a decrease in the flow conductance of the micro flow model, due to capillary blockage of channels. Since this capillary blockage was the main cause of the buildup of the viscous pressure contribution, it follows that this effect was strongest in the micro flow model with the lowest connectivity (model M4).

When the oil reached the outlet of the model, the breakthrough point was reached. After breakthrough, the influence of the outlet chamber becomes important. If one introduces a narrow outlet chamber in the model, it influences the pressure response directly. The single-phase flow conductance will be controlled by the narrow chamber at the end and in two-phase flow the capillary pressure will be determined by the high entry pressure of the narrow chamber. Therefore we have chosen large outlet chambers, which have a negligible influence on flow conductance and capillary pressures. This has a disadvantage, viz., that the oil that enters the outlet chamber will either remain connected or ''snap off,'' which is readily influenced by processes occurring outside the micro flow model that are hard to control. We have not included these effects in our network model, and therefore the results from simulations may deviate from those of the experiments after breakthrough. Our main interest is centered, however, on the pressure curves *before* breakthrough.

The flow rates were chosen in such a way that the viscous pressure drop was of the same order of magnitude as the capillary pressure difference. This regime is the most difficult one to describe by simulation, and it is therefore a good test to determine whether our model is satisfactory.

V. RESULTS AND DISCUSSION

We present here a selection of the experiments that were performed. Since our focus is on the pressure buildup during drainage, we have not always shown saturation profiles. For each of the models we also performed a single-phase flow experiment with water, to test our description of the micro flow model. We know that the channel depth is the most important parameter for single-phase flow. We therefore checked whether the single-phase pressure drops were simulated accurately when using our best estimate for the channel depth. These parameters were also used in the two-phase simulations.

Model M1. In the single-phase flow test the pressure drop over the micro flow model was found to be 38 mbar at a flow rate of 100 μl/min. According to our simulator, this was consistent with the value of 35 μm for the channel depth, which is the main parameter for single-phase flow. For drainage, we have shown the pressure curve, using *n*-decane and a displacement rate of 3 μl/min (Fig. 8). The curve follows

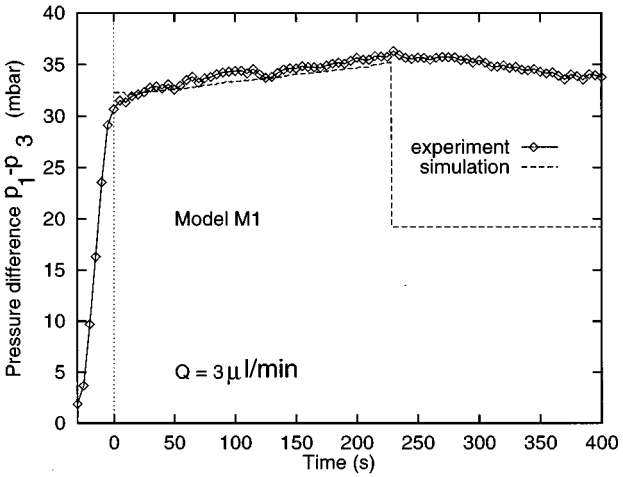

FIG. 8. The experimental and simulated pressure curve for drainage with *n*-decane in model M1.

the general pattern sketched in the previous section. First the pressure rises to the level of the entry pressure of the channels. During the displacement of water by oil, the pressure continues to rise. The oil and the water have equal viscosities in this case, and it is therefore not obvious what causes this rise. The simulation describes both the entry pressure and the pressure buildup accurately. By using the simulator we could interpret the pressure increase during displacement as being due to ''capillary blockage'' of many channels. A picture of the micro flow model during drainage is given in Fig. 9. This can be compared (on a *statistical* basis) with Fig. 10, where we show the simulated drainage front. The pressure drop after breakthrough differs for the simulation. This is explained at the end of Sec. IV.

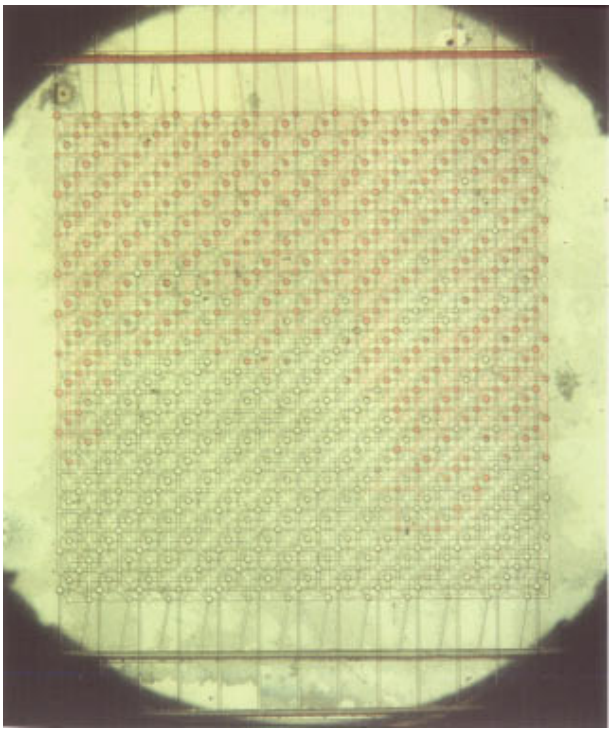

FIG. 9. (Color). A picture of model M1 during drainage.

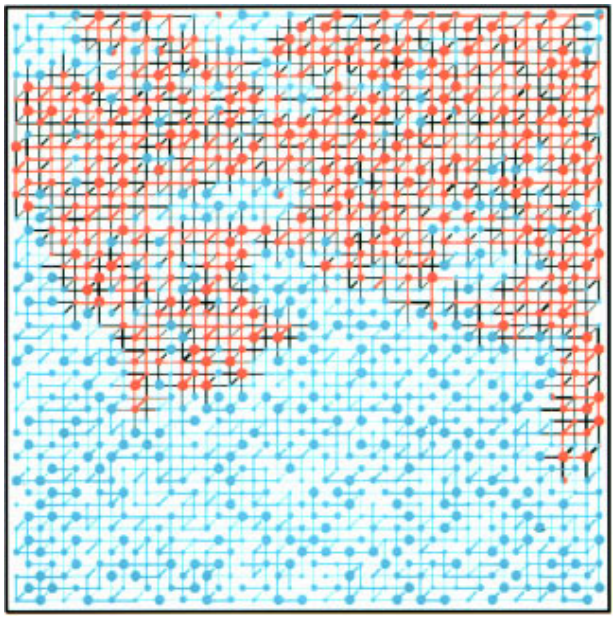

FIG. 10. (Color). The simulated drainage front in model M1.

Model M2, n-decane. The pressure drop over the model in a single-phase flow test was 6 mbar at 100 μl/min, which could be reproduced in a simulation, assuming a channel depth of 2×30 μm. For this model we have reported drainage experiments with *n*-decane and experiments with Vitrea-9 as the nonwetting phase. For drainage with *n*-decane at 10 μl/min, the comparison between simulation and experiment is illustrated in Fig. 11.

Model M2, Vitrea-9. Figures 12 and 13 give the results for a relatively slow drainage (1 μl/min) with Vitrea-9, whereas Figs. 14 and 15 show a faster drainage experiment (10 μl/min). The rise in pressure difference during drainage is still modest in the slower experiment, despite the much higher viscosity of Vitrea-9. The simulation curve follows the experimental one. During the fast experiment, however, there was a considerable build-up of pressure, which is underestimated by roughly a factor of 2 if the simulator is used. The simulated saturation front moving through the system is,

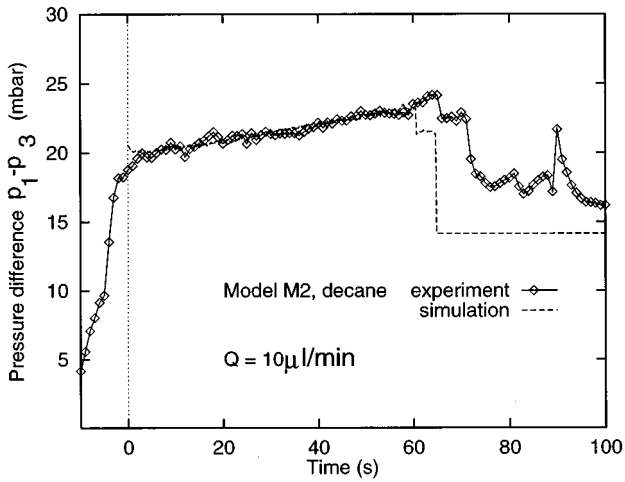

FIG. 11. The experimental and simulated pressure curve for fast drainage with *n*-decane in model M2.

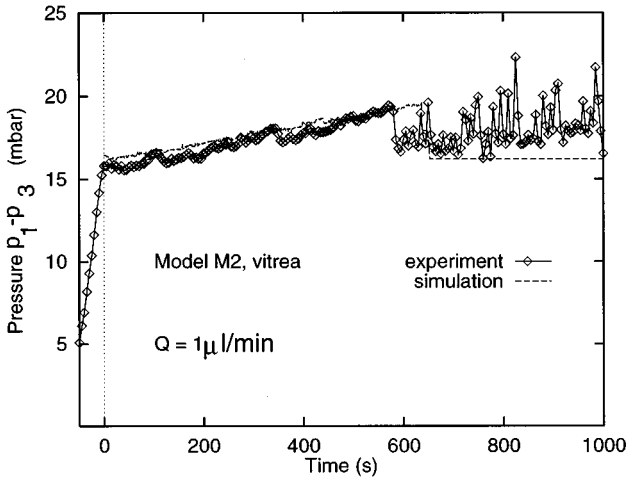

FIG. 12. The experimental and simulated pressure curve for slow drainage with Vitrea-9 in model M2.

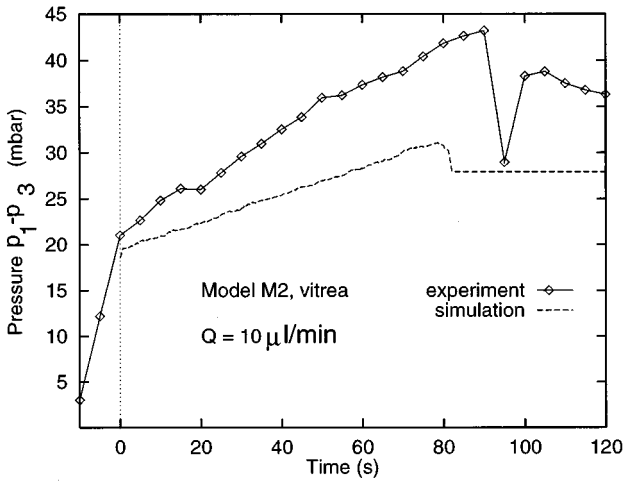

FIG. 14. The experimental and simulated pressure curve for fast drainage with Vitrea-9 in model M2.

however, comparable to the experimental one. Note that in this case the pressure increase during displacement could, in principle, be due to the higher viscosity of the oil. However, based on our single-phase flow measurement, we would expect a pressure drop of roughly 6 mbar for Vitrea-9 flow at 10 μl/min through the model. As Fig. 14 shows, the pressure increase is much larger, and therefore we have to introduce ''capillary blockage'' once again to explain the results.

Model M3. The pressure drop for single-phase flow, 11 mbar at 100 μl/min, was consistent with a channel depth of 35 μm. For two-phase flow, Fig. 16 shows that this model had two distinctly different entry pressures, i.e., the one for the pores and the one for the channels. This occurred because the pores had been etched in both glass plates, but the channels only in one glass plate. First all the pores at the entrance were filled, and then the channels ''after'' the pores. The experimental pressure curve and saturation curve (Fig. 17) are comparable with the simulation.

Model M4. There was an uncertainty in the channel depth in this model, because the model had been in the oven too long during the fusion. We used a single-phase flow test to calibrate this depth. The pressure drop during single-phase flow at 100 μl/min was found to be 25 mbar, which was consistent with a channel depth of 2×20 μm. For slow drainage (1 μl/min) with *n*-decane, the comparison between experiment and simulation is presented in Fig. 18. A higher injection rate (10 μl/min) gives rise to a large viscous pressure difference during drainage (Fig. 19). Again the pressure increase during displacement is much larger than the pressure drop for single-phase flow at 10 μl/min (i.e., $\sim$2.5 mbar). The low connectivity of the model (coordination number $\sim$3) is the underlying reason for the large pressure rise. When during drainage a number of the channels become capillary blocked, the remaining number of active

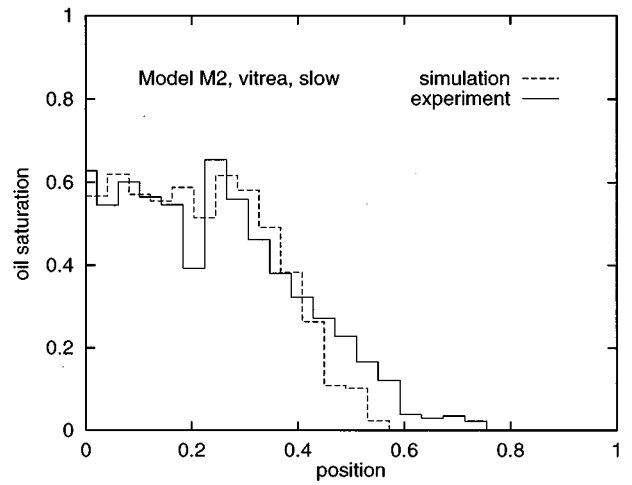

FIG. 13. The oil saturation as a function of the position in model M2, during slow drainage with Vitrea-9. Position 0 corresponds to the oil inlet at the top of the model, and position 1 to the outlet at the bottom.

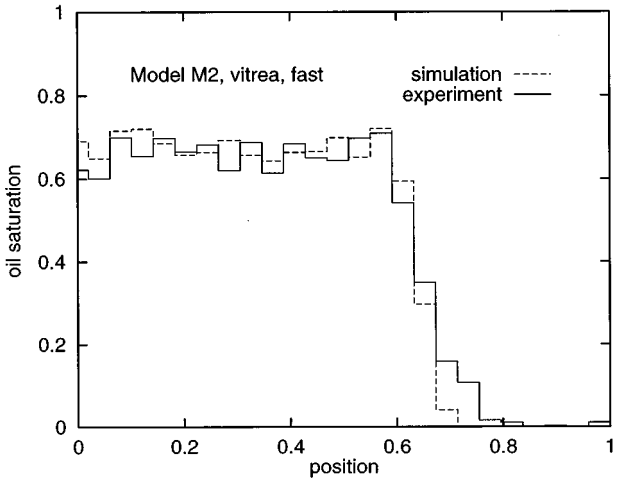

FIG. 15. The oil saturation as a function of the position in model M2, during fast drainage with Vitrea-9. Position 0 corresponds to the oil inlet at the top of the model, and position 1 to the outlet at the bottom.

TABLE II. The update rules.

	$S_j<S_e$	$S_e\leqslant S_j\leqslant S_f$	$S_j>S_f$
$S_i<S_e$	W[a]	O2[b]	B2[c]
$S_e\leqslant S_i\leqslant S_f$	O1[d]	O3[e]	B2
$S_i>S_f$	B1[f]	B1	O4[g]

[a]W: Use Eq. (B2). The fluid in the channel is water.
[b]O2: If oil flowed through the channel in the previous time step, use Eq. (B4). Otherwise use Eq. (B2) with water as the fluid in the channel.
[c]B2: Use Eq. (B4).
[d]O1: If oil flowed through the channel in the previous time-step, use Eq. (B3). Otherwise use Eq. (B2) with water as the fluid in the channel.
[e]O3: Use Eq. (B2). If oil flowed through the channel in the previous time step, the fluid in the channel is oil. Otherwise the fluid in the channel is water.
[f]B1: Use Eq. (B3).
[g]O4: If oil flowed through the channel in the previous time step, use Eq. (B2) with oil as the fluid in the channel. Otherwise use Eq. (B5).

flow paths is low. Therefore the pressure mounts. The simulation curve follows the experimental one, although in the simulation, breakthrough takes place slightly earlier.

Having discussed the experimental and simulation results, we can now show that the changes in the simulation rules (compared to Lenormand's work [24,25]) have improved the description of the pressure curves. As an example we use the 10 μl/min experiments in model M3, Fig. 16. The pressure curves for these experiments are reproduced by our simulations. With the simpler rules as explained at the end of Appendix B, the pressure buildup during the displacement is severely underestimated by the simulator; see Fig. 20. We have also simulated with the simple rules at an even higher injection rate, to see at which rate the old simulator would give a pressure buildup similar to that in the experiments. This occurred at a ten times higher rate, viz., 100 μl/min. However, at this rate, the overall pressure level is roughly 11 mbar higher, because of the single-phase pressure drop. It is clear, therefore, that although the old simulations also describe a transition to a viscous pressure regime, this transition takes place at too high flow rates. We conclude that in order to simulate two-phase flow correctly, one has to use our new simulation rules.

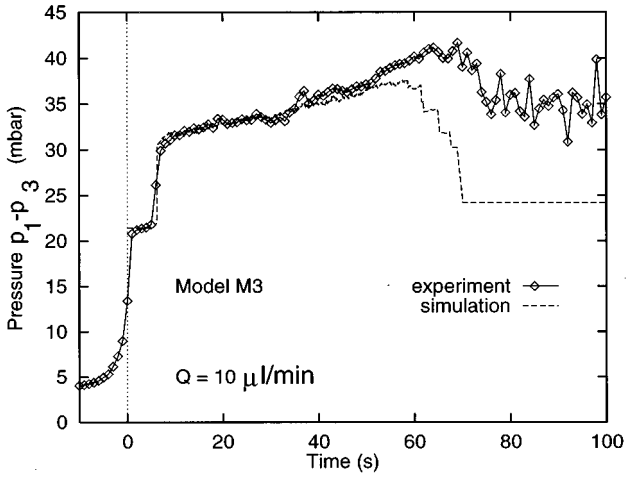

FIG. 16. The experimental and simulated pressure curve for drainage with *n*-decane in model M3.

We have shown that our experiments and simulations are in good agreement with each other, both for pressures and saturations, when $\mu_o/\mu_w=1$. We have used micro flow models with different topologies and various displacement rates. However, when comparing the experiment with the simulations for $\mu_o/\mu_w=12$, we are faced with a lack of agreement. Since in our case the oil is more viscous than water, the displacement has a stable front. This differs from the situation where the displacing phase is much less viscous than the defender phase, and viscous fingering occurs. The assumption that the case $\mu_o/\mu_w=12$ is more easy to model because the displacement front is stable does not follow from our results.

There are a few elements in our modeling that can be blamed for the lack of agreement. We would like to mention one of them in particular. During the pressure calculation in the network, the viscosity of the fluid in a channel must be known. In our model we cannot always say which fluid is present in a channel at an intermediate stage of the calculation (see Appendix B). Therefore we had to introduce an effective viscosity, Eq. (B7), which is essentially an average viscosity. We have tested the influence of averaging $1/\mu$ instead of μ. Although the pressure buildup during drainage was slightly larger (1 or 2 mbar) when introducing an average $1/\mu$, the picture did not change significantly. Neverthe-

TABLE III. The oil saturation at steady state as a function of the injection rate Q and $S_e=\tilde{S}$ and $S_f=1-\tilde{S}$ (see text).

	$\tilde{S}=0.01$	$\tilde{S}=0.05$	$\tilde{S}=0.10$	$\tilde{S}=0.20$	$\tilde{S}=0.25$
Q (μl/min)	Oil saturation at steady state				
0.1	0.69	0.69	0.68	0.67	0.65
0.3	0.69	0.69	0.69	0.67	0.67
1.0	0.74	0.73	0.70	0.71	0.66
3.0	0.78	0.78	0.74	0.72	0.69
10.0	0.85	0.84	0.82	0.78	0.75
30.0	0.89	0.88	0.85	0.81	0.77
100.0	0.94	0.93	0.90	0.85	0.81

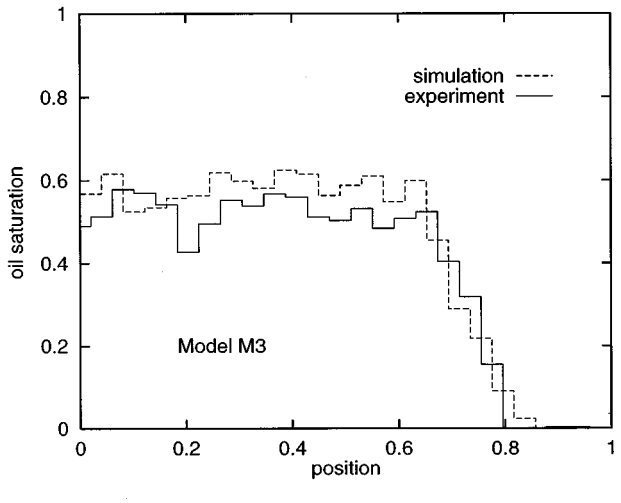

FIG. 17. The oil saturation as a function of the position in model M3, during drainage with *n*-decane. Position 0 corresponds to the oil inlet at the top of the model, and position 1 to the outlet at the bottom.

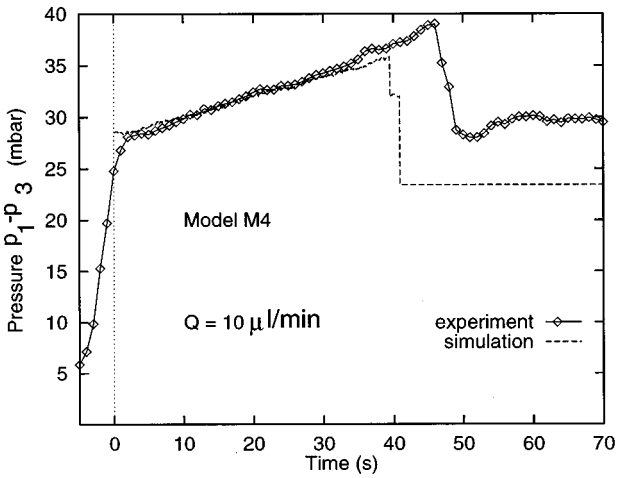

FIG. 19. The experimental and simulated pressure curve for fast drainage with *n*-decane in model M4.

less we feel that improvements in these rules for unequal viscosities are possible and that such improvements would contribute to a better agreement between experiment and simulation.

In summary, we have developed a simulator that describes the interaction between capillary and viscous effects in drainage. We have performed experiments using micro flow models to establish the validity of the simulator. The simulations are in agreement with the experiments for the decane-water system, where the viscosity ratio is 1. There is a discrepancy, however, between the simulations and the experiments, when the viscosity of the nonwetting phase is much higher than the viscosity of the wetting phase. This discrepancy occurs for measurements in the same model (M2) and with the same displacement rate (10 μl/min) for which there is good agreement when using a fluid system with equal viscosities. Therefore we conclude that the simulator produces results that are comparable to experimental results for equal viscosities, but that there is room for improvement when there is a large contrast in viscosities.

ACKNOWLEDGMENTS

We would like to thank W. van der Brugghen, who developed the method for making micro flow models and initiated the experimental setup. We would also like to thank D.O.E. Gebhardt for critically reading the manuscript.

APPENDIX A: FLOW PROPERTIES OF THE CHANNELS

In this Appendix we demonstrate the flow properties of the channels that were used in the network simulations as shown in this article. Two properties were made use of in the network simulator: the flow conductance and the capillary entry pressure. Both of these depend on the geometry and the size of the channels. In the network simulator we have introduced a geometry that resembles the shape of an etched

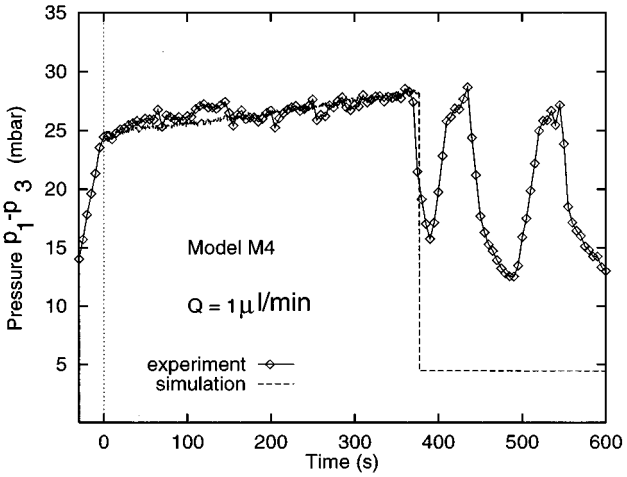

FIG. 18. The experimental and simulated pressure curve for drainage with *n*-decane in model M4.

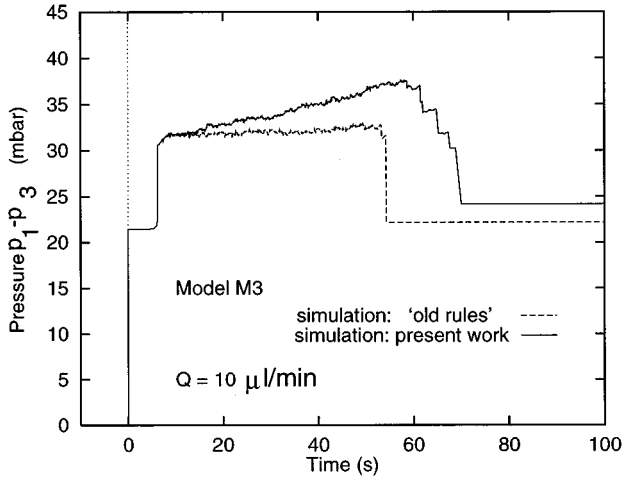

FIG. 20. Simulations of drainage in model M3 with *n*-decane at 10 μl/min, using both the old simulations rules and the proposed new ones.

channel, as depicted in Fig. 1.

The flow conductance c_{ij} of a channel connecting pores i and j is defined by Eq. (1). For the calculation of c_{ij} it was assumed that the flow in the channel is of the Poiseuille type. For a cylindrical channel the flow conductance as given in any text book on fluid dynamics [29] is $c_{ij}=\pi d^4/(128l)$. However, for channels as in Fig. 1 no analytical formula is known, so the flow conductance as a function of $(w-2d)/d$ was computed numerically using a finite difference scheme. In the network simulation these results were obtained with

$$c_{ij}=\frac{d^4}{l}\sum_{i=0}^{6} C_i\left(\frac{w-2d}{d}\right)^i, \tag{A1}$$

where l is the length of the channel, and the coefficients C_i are

$$\begin{aligned} C_i = {} & 0.0744583414,\ 0.0775210038,\ 0.0134347430,\\ & -0.0139011050,\ 0.0071067621,\\ & -0.0017048067,\ 0.0001533872,\ \text{for}\ i=0,\ldots,6. \end{aligned}$$

This fit is valid for $(w-2d)/d\in[0,4]$. Outside this range it is better to use as an approximation the flow conductance of a rectangular channel [29] with the same depth d and a width $\tilde{w}$ such that the cross-sectional area for flow remains the same, i.e., $\tilde{w}=w+\pi d/2$.

The capillary entry pressure P_{ij}^e of a channel is the pressure difference needed between the nonwetting and wetting phase for the former to enter the channel. For a cylindrical channel geometry this pressure difference is given by $P_{ij}^e=4\sigma\cos\vartheta/d$, where σ is the interfacial tension between the fluids, ϑ the contact angle, and d the diameter of the cylinder. In Ref. [30] a method is given to calculate the entry pressure for more complicated channel geometries. We have applied this method to the type of channel used in our network simulator. The result is

$$P_{ij}^e=\frac{\sigma}{d}\min_{\psi\in[0,1/4\pi]}\left(\frac{L_{nw}(\psi)+L_{ns}(\psi)\cos\vartheta}{A(\psi)}\right), \tag{A2}$$

where the functions L_{nw}, L_{ns} and A are given by

$$L_{nw}(\psi)=\frac{(1/2)\,\alpha}{(\sin 1/2)\,\alpha}(1-\tan^2\psi)\cos\psi, \tag{A3}$$

$$L_{ns}(\psi)=(w-2d)/d+\tan\psi+2\psi, \tag{A4}$$

and

$$\begin{aligned} A(\psi)=\frac{w-2d}{2d}+\psi+\frac{1}{2}\tan\psi\cos(2\psi)+\frac{1}{8}\left(\frac{\alpha-\sin\alpha}{\sin^2(1/2)\,\alpha}\right)\\ \times(1-\tan^2\psi)^2\cos^2\psi. \end{aligned} \tag{A5}$$

Here, $\alpha=\pi-2\vartheta-2\psi$. The minimization was performed numerically.

APPENDIX B: NETWORK EQUATIONS AND UPDATE RULES

In Sec. II we have explained how one can construct the flow equations for two-phase flow in a network. We will now work them out in more detail. For each pore labeled as i one has [see Eq. (8)]

$$Q_i^e=\sum_j Q_{ij}. \tag{B1}$$

The expression that has to be used for Q_{ij} depends (1) on which fluid is present in the channel connecting pores i and j and (2) on whether menisci are present in the channel. In Eqs. (4)–(7) we have given the three possible expressions for Q_{ij}. Notice that Eq. (5) can have two forms depending on whether pore i or pore j is filled with oil. In the expression of Eq. (5) it was assumed that pore i is filled with oil. If pore j is filled with oil and pore i with water, one has to exchange i and j in Eq. (5) and use $Q_{ji}=-Q_{ij}$ and $P_{ji}^e=P_{ij}^e$ (c_{ij} and μ_{ij} are also symmetric). Therefore, Q_{ij} in Eq. (B1) can have four forms:

(1) No meniscus is present in the channel:

$$Q_{ij}=\frac{c_{ij}}{\mu_{ij}}\Delta_{ij}. \tag{B2}$$

(2) One meniscus is present, pore i is filled with oil, pore j is filled with water:

$$Q_{ij}=\frac{c_{ij}}{\mu_{ij}}\{\theta(\Delta_{ij}-P_{ij}^e)(\Delta_{ij}-P_{ij}^e)+\theta(\Delta_{ji})\Delta_{ij}\}. \tag{B3}$$

(3) One meniscus is present, pore i is filled with water, pore j is filled with oil:

$$Q_{ij}=\frac{c_{ij}}{\mu_{ij}}\{\theta(\Delta_{ji}-P_{ij}^e)(\Delta_{ij}+P_{ij}^e)+\theta(\Delta_{ij})\Delta_{ij}\}. \tag{B4}$$

(4) Two menisci are present, pores i and j are filled with oil, and the channel is filled with water:

$$Q_{ij}=\frac{c_{ij}}{\mu_{ij}}\{\theta(\Delta_{ij}-P_{ij}^e)(\Delta_{ij}-P_{ij}^e)+\theta(\Delta_{ji}-P_{ij}^e)(\Delta_{ij}+P_{ij}^e)\}. \tag{B5}$$

The notation Δ_{ij} in Eqs. (B2)–(B5) represents

$$\Delta_{ij}=p_i-p_j-\rho_{ij}\mathbf{g}\cdot(\mathbf{x}_i-\mathbf{x}_j). \tag{B6}$$

Notice that $\Delta_{ji}=-\Delta_{ij}$. In Eq. (B2) we have used for μ_{ij} and ρ_{ij} the values of the viscosity and density of the fluid that is flowing through the channel (water or oil). In situations (2), (3), and (4) the identity of the fluid flowing through the channel (oil or water or capillary blocked) can only be determined after the pressure field in the whole network has been determined. Therefore, we have used in Eqs. (B3)–(B5) ''effective'' viscosities and densities for μ_{ij} and ρ_{ij}, which are defined by

$$\mu_{ij}=S_{ij}\mu_o+(1-S_{ij})\mu_w, \tag{B7}$$

$$\rho_{ij}=S_{ij}\rho_o+(1-S_{ij})\rho_w, \tag{B8}$$

where S_{ij} is the average of the oil saturations of pores i and j. Combining Eq. (B1) with Eqs. (B2)–(B5) the general form of the flow equations is given by

$$\begin{aligned}F_i(\mathbf{p})=&-Q_i^e+\sum_{ij\in(1)}\frac{c_{ij}}{\mu_{ij}}\Delta_{ij}+\sum_{ij\in(2)}\frac{c_{ij}}{\mu_{ij}}\{\theta(\Delta_{ij}-P_{ij}^e)\\&\times(\Delta_{ij}-P_{ij}^e)+\theta(\Delta_{ji})\Delta_{ij}\}+\sum_{ij\in(3)}\frac{c_{ij}}{\mu_{ij}}\{\theta(\Delta_{ji}-P_{ij}^e)\\&\times(\Delta_{ij}+P_{ij}^e)+\theta(\Delta_{ij})\Delta_{ij}\}+\sum_{ij\in(4)}\frac{c_{ij}}{\mu_{ij}}\{\theta(\Delta_{ij}-P_{ij}^e)\\&\times(\Delta_{ij}-P_{ij}^e)+\theta(\Delta_{ji}-P_{ij}^e)(\Delta_{ij}+P_{ij}^e)\}=0.\end{aligned} \tag{B9}$$

This is a set of nonlinear equations, which may be solved by a combination of an over-relaxation and a dampened Newton-Raphson method [31].

We need to specify how to decide which of the four equations (B2)–(B5) should be used for Q_{ij}. The decision has to be made each time after one has updated the saturations of the pores. For this purpose we have formulated the so-called ''update rules.'' These rules involve the saturations of the neighboring pores and the identity of the fluid that flowed through the channel during the previous time step (oil, water, or capillary blocked). Although there is some ambiguity as to how one should select these ''update rules,'' our choice seems to be ''reasonable.''

In the update rules we have used two threshold saturations S_e and S_f ($S_e<S_f$). If we wish to establish which of the four equations (B2)–(B5) have to be applied for a channel connected to pores i and j, we must compare the oil saturations S_i and S_j of the pores with the threshold saturations. For some situations also the status of the channel in the previous time step (flowing oil or water, or capillary blocked) plays a role for the update rules. We have listed the update rules in Table II.

We still have to decide on the values for S_e and S_f. At present they are still completely arbitrary in the simulator. In principle one would like to relate them to a kind of ''residual oil'' (S_e) and ''connate water'' ($1-S_f$) saturations of a pore. So far we do not have such an interpretation, but based on experimental observations we have chosen S_e and S_f close to zero and one, respectively. In the simulations presented in this paper they were taken to be $S_e=0.05$ and $S_f=0.95$. We have performed simulations using several values for S_e and S_f on a fixed network realization. This gave information on the influence of these parameters.

TABLE IV. The simpler update rules as used in Refs. [24, 25]. Only in the lower-left corner and in the upper-right corner a capillary entry pressure P_c is taken into account. Depending on the local pressure field, the channel can be capillary blocked, or contain flowing water or oil. For the other cases, where no capillary pressure is involved, we indicate the type of fluid flowing through the channel. In two cases this depends on the local pressure field.

	$S_j<S_e$	$S_e\leqslant S_j\leqslant S_f$	$S_j>S_f$
$S_i<S_e$	Water	Water	P_c
$S_e\leqslant S_i\leqslant S_f$	Water	Water	Water or oil
$S_i>S_f$	P_c	Water or oil	Oil

In Table III we have listed the oil saturations at steady state as a function of $\tilde{S}$ and the injection flow rate Q. The fluid properties were $\mu_o=\mu_w=0.775$ mPa s, $\rho_w=995$, $\rho_o=721$ kg/m^3, and $\sigma=33.1$ mN/m. We took $S_e=\tilde{S}$ and $S_f=1-\tilde{S}$ for $\tilde{S}=0.01$, 0.05, 0.10, 0.20, and 0.25. From the table it is clear the the outcome of a simulation depends on the values of S_e and S_f. However, the dependence is not strong if $\tilde{S}$ is restricted to $\tilde{S}<0.10$. This seems reasonable from an experimental approach. If one wishes to avoid the usage of these arbitrary parameters, one would have to introduce dynamic mobilization and trapping criteria for oil. Therefore also the pores need to be given flow properties, which has not been done in the present investigation.

Finally, we discuss the difference with the approach of Lenormand *et al.* [24,25]. Lenormand *et al.* assumed that the interfacial tension only plays a role when two adjacent pores are completely filled by different fluids, i.e., when $S_i=0$ and $S_j=1$. In all other cases they used Poiseuille flow with an effective viscosity as in Eq. (B7). A table with the simpler update rules is shown as Table IV, to indicate the differences with the present work. This table can be compared with Table II. An advantage of the simpler rules is that one only needs to know the fluid content of the pores: the fluid in the channel between two pores is not relevant. However, we could not reproduce the experimental results with this approach, and therefore we introduced the fluid content of each channel as a modeling parameter.

In retrospect, having looked closely at our simulations, we can say that the most significant difference was the rule for flow between two oil-filled pores. In Refs. [24, 25] the rule was that in this case oil would flow in the channel, without capillary pressure terms. We concluded that it was important to model the effect of water still being present in the channel between the pores. This implies two interfaces and therefore two capillary pressure terms. This type of channel can become capillary blocked, which has quite a strong effect on the pressure buildup during drainage.

[1] A. E. Scheidegger, *The Physics of Flow through Porous Media* (University of Toronto Press, Toronto, 1974).

[2] F. A. L. Dullien, *Porous Media, Fluid Transport and Pore Structure* (Academic Press, New York, 1979).

[3] J. Koplik and T. J. Lasseter, *Proceedings of the Society of Petroleum Engineers 57th Annual Technical Conference* (SPE, New Orleans, 1982).

[4] J. Koplik, J. Fluid Mech. **119**, 219 (1982).

[5] J. Koplik and T. J. Lasseter, Chem. Eng. Commun. **26**, 285 (1984).
[6] A. R. Kerstein, J. Phys. A **16**, 3071 (1983).
[7] S. C. van der Marck, Phys. Rev. Lett. **77**, 1785 (1996).
[8] M. Blunt and P. King, Phys. Rev. A **42**, 4780 (1990); Transp. Porous Media **6**, 407 (1991).
[9] M. Blunt, M. J. King, and H. Scher, Phys. Rev. A **46**, 7680 (1992).
[10] P. G. de Gennes and E. Guyon, J. Méc. **17**, 403 (1978).
[11] R. Lenormand and C. Bories, C. R. Seances Acad. Sci., Ser. B **291**, 279 (1980).
[12] R. Chandler, J. Koplik, K. Lerman, and J. F. Willemsen, J. Fluid Mech. **119**, 249 (1982).
[13] D. Wilkinson and J. F. Willemsen, J. Phys. A **16**, 3365 (1983).
[14] R. Lenormand and C. Zarcone, Phys. Rev. Lett. **54**, 2226 (1985).
[15] T. A. Witten and L. M. Sander, Phys. Rev. Lett. **47**, 1400 (1981); Phys. Rev. B **27**, 5686 (1983).
[16] L. Paterson, Phys. Rev. Lett. **52**, 1621 (1984).
[17] J. D. Chen and D. Wilkinson, Phys. Rev. Lett. **55**, 1892 (1985).
[18] G. R. Jerauld and S. J. Salter, Transp. Porous Media **5**, 103 (1990).
[19] S. R. McDougall and K. S. Sorbie, in *Proceedings of the 3rd European Conference on the Mathematics of Oil Recovery*, edited by M. A. Christie *et al.* (Delft University Press, Delft, 1992).
[20] S. Bryant and M. Blunt, Phys. Rev. A **46**, 2004 (1992).
[21] S. L. Bryant, D. W. Mellor, and C. A. Cade, AIChE. J. **39**, 387 (1993).
[22] M. M. Dias and A. C. Payatakes, J. Fluid Mech. **164**, 305 (1986).
[23] G. N. Constantinides and A. C. Payatakes, J. Colloid Interface Sci. **141**, 486 (1991).
[24] R. Lenormand, C. Zarcone, and A. Sarr, J. Fluid Mech. **135**, 337 (1983).
[25] R. Lenormand, E. Touboul, and C. Zarcone, J. Fluid Mech. **189**, 165 (1988).
[26] D. G. Avraam and A. C. Payatakes, J. Fluid Mech. **293**, 207 (1995).
[27] K. Aziz and A. Settari, *Petroleum Reservoir Simulation* (Applied Science Publisher, London, 1979).
[28] Shell Product Datasheet ''*Vitrea*,'' Shell International Chemicals Company.
[29] J. Happel and H. Brenner, *Low Reynolds Number Hydrodynamics; With Special Applications to Particulate Media* (Noordhoff, Leiden, 1973).
[30] R. P. Mayer and R. A. Stowe, J. Colloid Sci. **20**, 893 (1965).
[31] J. Ortega and W. Rheinboldt, *Iterative Solution of Nonlinear Equations in Several Variables* (Academic Press, New York, 1970).